Journal of Computational Physics 290 (2015) 298–317

Contents lists available at ScienceDirect

Journal of Computational Physics

www.elsevier.com/locate/jcp

A discrete element based simulation framework to investigate particulate spray deposition processes

Debanjan Mukherjee *, Tarek I. Zohdi

Department of Mechanical Engineering, University of California, Berkeley, United States

ARTICLE INFO

Article history:
Received 9 May 2014
Received in revised form 6 February 2015
Accepted 7 February 2015
Available online 2 March 2015

Keywords:
Particle deposition
Particle collisions
Spray dynamics
Discrete element method

ABSTRACT

This work presents a computer simulation framework based on discrete element method to analyze manufacturing processes that comprise a loosely flowing stream of particles in a carrier fluid being deposited on a target surface. The individual particulate dynamics under the combined action of particle collisions, fluid–particle interactions, particle–surface contact and adhesive interactions is simulated, and aggregated to obtain global system behavior. A model for deposition which incorporates the effect of surface energy, impact velocity and particle size, is developed. The fluid–particle interaction is modeled using appropriate spray nozzle gas velocity distributions and a one-way coupling between the phases. It is found that the particle response times and the release velocity distribution of particles have a combined effect on inter-particle collisions during the flow along the spray. It is also found that resolution of the particulate collisions close to the target surface plays an important role in characterizing the trends in the deposit pattern. Analysis of the deposit pattern using metrics defined from the particle distribution on the target surface is provided to characterize the deposition efficiency, deposit size, and scatter due to collisions.

1. Introduction

This paper addresses the problem of deposition of colliding and flowing particulate media onto a specified target surface, and an analysis of the behavior of the resulting deposit pattern. This is an aspect of major interest in a broad variety of modern industrial processes, particularly in the context of spray forming and additive manufacturing processes. Extensive review of the state of the art for a broad range of such processes can be found in [1], and [2]. Specifically for detailed discussion on particle deposition and aggregation phenomena, the reader is referred to [3], and [4]. The applications of particle spray and deposition processes encompasses a wide gamut of areas including design of functionally engineered surfaces (see for example [5,6]), additive manufacturing technologies (see for example [7–9]), patterning and fabrication using inkjet printing (see for example [10,11]), and biomedical applications (see for example [12,13]). It is evident from the diversity of such applications that these are fundamentally coupled multi-physical processes, and obtaining information on the synergistic interplay between the various physical phenomena that govern these processes is an important issue. In general these physical interactions include a combination of fluid–particle interactions, particle-interactions with a collection of surfaces that bound the domain of the flow, inter-particle collisional interactions, and adhesive and physical bonding interactions. In this work, we present a computer simulation framework that is based on collision driven discrete element method to investigate the overall process behavior of a typical particle spray process. Our computational abstraction of such

* Corresponding author.
E-mail addresses: debanjan@berkeley.edu (D. Mukherjee), zohdi@me.berkeley.edu (T.I. Zohdi).

http://dx.doi.org/10.1016/j.jcp.2015.02.034
0021-9991/

processes involves a collection of particles released in a specified manner from a fixed region in space, being propagated towards a target surface by a carrier fluid media, and deposited on the target surface.

A detailed overview of thermal spray process modeling and simulations – with emphasis on the droplet dynamics during deposit solidification can be found in [14], and similar other investigations for thermal sprays can also be found in the works by [15,16], and [17] amongst other recent works. The computational modeling of particle deposition under the action of a carrier fluid has been also studied by researchers in various contexts and using various techniques. For example, deposition of aerosol particles in a channel flow has been studied by [18], sub micron size particle dispersion in channel flows has been studied by [19], particle deposition in turbulent boundary layers using Lagrangian random-walk approach has been studied by [20], and a similar approach for near-wall flows has been used in a study by [21]. However, not much focus has been directed towards higher particle number densities, the effect of inter-particle collisions on the deposit pattern properties, and on the near-target build up of particles. For guided particle sprays, and for target deposit quality inter-particle collisions can cause substantial scattering in the pattern of particle incidence on the specified target site. Discrete element methods (see [22,23] for details) for modeling coupled spray dynamics and deposit growth provide the ability to explicitly track all inter-particle and particle-target collisions and hence provide a suitable alternative. Discrete element techniques for simultaneous flow dynamics, and growth and microstructure evolution are relatively recent - and some related existing studies include the work on event-driven particle deposit growth by [24], and on charged particle cluster impact with a target surface by [25]. Particularly in the work by [24], a collision based approach was used to incorporate particle rebound from the growing deposit pattern. In-flight dynamics of the collection of particles under the combined action of fluid–particle and particle–particle interactions have been formulated in the present framework in combination with the dynamics of the deposit growth at the target surface, to achieve a systemwide behavior of the process with regards to various parameters that govern the particle incidence pattern on the target surface.

The organization of the rest of the paper is as follows: Section 2 details the various physical models at the level of the individual discrete particles, Section 3 details in particular the considerations for deriving an appropriate model for deposit adhesion, Section 4 outlines the hierarchical assembly of the particle level models, and appropriate boundary conditions into the overall computer simulation framework, Section 5 presents detailed numerical examples and analysis to highlight the utility of such a framework in capturing physical behavior of the system. Throughout the ensuing discussions, the term particles will be used to represent the mathematically abstracted computational units that comprise the discrete medium in the flow (also called discrete elements). With regards to applicability in some of the various applications presented earlier, these could be representative of not only actual particles, but also meso-scopic idealized computational units. The work presented here is part of an ongoing effort towards developing a general-purpose computer simulation tool to analyze the dynamics of particulate and granular media in engineering applications. All dynamics simulations were found to be reasonable in performance time.

2. Physical models for particle-level interactions

2.1. Particle–particle contact interactions

The principal governing physical interactions for the dynamics of the particle streams are the particle–particle and particle–surface contact interactions. Owing to the underlying rigidity of the individual particles that comprise the particle streams, these systems are collisionally dominant. There exist a wide range of approaches for characterizing the force between contacting bodies, and a comprehensive review of all the approaches will be beyond the scope of the current work. The interested reader is referred to the classical work of [26], and the extensive reviews on contact force models presented by [22], and [27]. A very commonly used approach is to characterize the contact force between two bodies based on a geometric overlap that characterizes the contact deformation. For two spherical bodies of radii R_1 and R_2 (located at $\mathbf{r}_1$ and $\mathbf{r}_2$ respectively), this overlap is easily estimated by $\delta_n = \|\mathbf{r}_1 - \mathbf{r}_2\| - (R_1 + R_2)$. Obviously for positive values of δ_n, there is no contact occurring between the two bodies – which forms a direct check for contact detection. Perhaps the most fundamental of these models is the Hertzian model for normal contact (see [28] and [26]), which relates the normal contact force to the normal contact overlap as:

$$F_c^n = \frac{4}{3}\sqrt{R}E^*\delta_n^{3/2} = K_n\delta_n^{3/2}$$

where $\delta_n = \|\mathbf{r}_1 - \mathbf{r}_2\| - (R_1 + R_2)$ is the relative deformation that they undergo, $1/R = 1/R_1 + 1/R_2$, and the effective elasticity E^* is defined as $\frac{1}{E^*} = \frac{1-\nu_1^2}{E_1} + \frac{1-\nu_2^2}{E_2}$, where ν and E denote the Poisson's ratio and elasticity of the contacting particles. Similar models have also been presented by [29–33], and [22] amongst others. The implementation of these models in a computer simulation framework for resolving the particle dynamics requires the numerical time-steps to be lesser than the total duration of the contact. While this is required for physically correct representations of systems with enduring contacts (that is, with significant contact-durations as compared to the characteristic time-scales of the particle system), for collisionally dominant systems with non-enduring contacts of significantly small durations, this may lead to very stringent requirements on the numerical time-step sizes.

Alternatively, a direct pairwise balance of linear and angular momenta for a collection of contacting particles can be used to derive an estimate of the contact forces. This approach has been used for flowing particulate media in the works of Zohdi

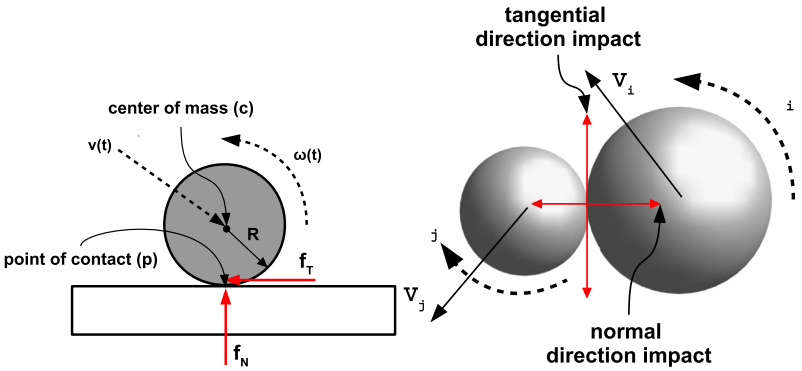

Fig. 1. Schematic of a typical particle–surface contact configuration (left) and particle–particle contact configuration (right) used to derive the collisional interactions using a balance of linear and angular momenta.

et al. (see [34–37] for details). For applications involving dynamic systems of particles undergoing non-enduring contacts, this provides a theoretically consistent estimate of the contact interactions. Furthermore, this approach does not require an explicit force deformation relation to be evaluated and integrated over the duration of the contact – thereby relaxing the restrictions on the time-step sizes to be lesser than contact duration.

In order to outline the expressions for the forces obtained using a direct balance of momenta, we refer to the schematic representations of inter-particle and particle–surface contacts as presented in Fig. 1. For particle–particle collisions, we define normal vectors for the pairwise collisions as follows:

$$\hat{\mathbf{n}}_{ji} = \frac{\mathbf{r}_j - \mathbf{r}_i}{\|\mathbf{r}_j - \mathbf{r}_i\|} \qquad \hat{\mathbf{n}}_{ij} = \frac{\mathbf{r}_i - \mathbf{r}_j}{\|\mathbf{r}_i - \mathbf{r}_j\|} \tag{1}$$

Assuming the particles are idealized to be rigid (that is, any contact deformations that occur are neither permanent nor significant as compared to the particle dimensions), the velocities at the point of contact for each spherical particle can thus now be written as:

$$\mathbf{v}_{pi} = \mathbf{v}_{ci} + \omega_i \times (R_i \hat{\mathbf{n}}_{ji}) \tag{2}$$

$$\mathbf{v}_{pj} = \mathbf{v}_{cj} + \omega_j \times (R_j \hat{\mathbf{n}}_{ij}) \tag{3}$$

The relative velocity at the point of contact can be defined as $\mathbf{v}_{rel} = \mathbf{v}_{pj} - \mathbf{v}_{pi}$. Using the relative velocity at the contact point, the direction of tangential slip can be characterized by a unit vector $\hat{\mathbf{t}}_{ij}$ as follows:

$$\hat{\mathbf{t}}_{ij} = \frac{\mathbf{v}_{rel} - (\mathbf{v}_{rel} \cdot \hat{\mathbf{n}}_{ij})\hat{\mathbf{n}}_{ij}}{\|\mathbf{v}_{rel} - (\mathbf{v}_{rel} \cdot \hat{\mathbf{n}}_{ij})\hat{\mathbf{n}}_{ij}\|} \tag{4}$$

The pairwise linear momentum balance for the collision of the particles can now be written as:

$$m_i \mathbf{v}_i(t + \delta t) - m_i \mathbf{v}_i(t) = \langle \mathbf{F}_i^c \rangle \delta t + \langle \mathbf{F}_i^e \rangle \delta t \tag{5}$$

$$m_j \mathbf{v}_j(t + \delta t) - m_j \mathbf{v}_j(t) = \langle \mathbf{F}_j^c \rangle \delta t + \langle \mathbf{F}_j^e \rangle \delta t \tag{6}$$

where superscripts 'c' and 'e' denote contact forces and external, non-contact forces respectively, and $\langle \cdot \rangle$ denotes the averaged impulse over the collision duration δt. While the contact deformations are assumed negligible, in reality the work done by the mechanical forces within the bulk of the contact particles owing to any inelastic deformations leads to a dissipation of energy. This can be accounted for using the restitution coefficient (e). Decomposing the overall contact event into a compression phase where particles approach each other, followed by a recovery phase where particles recede from each other, the restitution coefficient (e) can be defined as the ratio between the contact impulse during recovery phase to that during compression phase. Assuming further that the total contact force for the pairwise collision on particle i can be written as $\mathbf{F}_i^c = f_N \hat{\mathbf{n}}_{ij} + f_T \hat{\mathbf{t}}_{ij}$, and performing some algebra the total normal contact force can be written as follows:

$$\begin{aligned} \langle f_N \rangle \delta t &= \langle f_N \rangle_C \delta t_1 + \langle f_N \rangle_R (\delta t - \delta t_1) = (1 + e) \langle f_N \rangle_C \delta t_1 \\ &= \frac{1 + e}{m_i + m_j} \left[m_i \langle F_{jn}^e \rangle_C \delta t_1 - m_j \langle F_{in}^e \rangle_C \delta t_1 \right] - \frac{(1 + e) m_i m_j}{m_i + m_j} \left[v_{in}(t) - v_{jn}(t) \right] \end{aligned} \tag{7}$$

where $\langle \cdot \rangle_C$, $\langle \cdot \rangle_R$ denote impulse over compression and recovery phases respectively. The interested reader is referred to Appendix A for mathematical details. The contact impulse can now be plugged back into the linear momentum balance equations to get the respective post collisional velocity updates as follows:

$$m_i v_{in}(t+\delta t) = m_i v_{in}(t) + \frac{1+e}{m_i+m_j}\left[m_i\langle F^e_{jn}\rangle_C \delta t_1 - m_j\langle F^e_{in}\rangle_C \delta t_1\right] - \frac{(1+e)m_i m_j}{m_i+m_j}\left[v_{in}(t) - v_{jn}(t)\right] + \langle F^e_{in}\rangle \delta t \tag{8}$$

$$m_j v_{jn}(t+\delta t) = m_j v_{jn}(t) - \frac{1+e}{m_i+m_j}\left[m_i\langle F^e_{jn}\rangle_C \delta t_1 - m_j\langle F^e_{in}\rangle_C \delta t_1\right] + \frac{(1+e)m_i m_j}{m_i+m_j}\left[v_{in}(t) - v_{jn}(t)\right] + \langle F^e_{jn}\rangle \delta t \tag{9}$$

For the tangential component of the contact impulses, the momentum balance in $\hat{\mathbf{t}}_{ij}$ (see Eq. (4)) can be used along with a Coulomb stick-slip criteria, to derive expressions for the impulse. The inherent discontinuity of the stick-slip law can lead to mathematical complications, thereby requiring rigorous numerical techniques to handle such a model within the rigid body assumption for contact force calculation. An extensive review of the techniques available can be found in [38]. The latest developments, as discussed in the review, incorporate the idea of impulsive forces in rigid body dynamics as measures of distributions instead, and the idea of combining rigid body contact problems with an area of convex analysis called the linear complementarity problem (for mathematical foundations of the method see the text by [39]). However, the implementation of such a formulation into the time-discretized motion equations for a system of particles can be a complex task, as discussed by [38]. For systems of flowing particles with non-enduring contacts the system behavior is not significantly dependent on the exact stick-slip nature of the contact friction, as opposed to more static, enduring contacts (see for example the discussion [40], and [22]). Therefore, for the applications of interest in this paper, the exact determination of stick-slip friction in an impulse–momentum balance type contact formulation can be replaced by a simple regularization of the discontinuous Coulomb friction law. Such regularized friction models can lead to robust numerical methods for integrating the motion equations. Discussions on the models for regularized Coulomb friction can be found in the works by [41], and by [42], and in general, the friction force can be given by:

$$\langle f_T\rangle = \mu\mathcal{R}\left(v_{slip,t}\right)\|f_N\| \tag{10}$$

where $\mathcal{R}\left(v_{slip,t}\right)$ is a regularization function that approximates the discontinuity of the stick-slip criteria. A commonly used form of the regularization function $\mathcal{R}$ can be given as follows:

$$\mathcal{R}_1\left(v_{slip,t}\right) = \begin{cases} -1 & \forall v_{slip,t} < -\epsilon \\ \frac{v_{slip,t}}{2\epsilon} & \forall -\epsilon \le v_{slip,t} \le \epsilon \\ 1 & \forall v_{slip,t} > \epsilon \end{cases} \tag{11}$$

where ϵ is a regularization parameter, and smaller values of this parameter lead to better approximations of the stick-slip friction law. The tangential velocity updates can now be given using the tangential component momentum balance as follows:

$$m_i v_{it}(t+\delta t) = m_i v_{it}(t) + \mu\mathcal{R}\left(v_{slip,t}\right)\|f_N\|\delta t + \langle F^e_{it}\rangle \delta t \tag{12}$$

$$m_j v_{jt}(t+\delta t) = m_j v_{jt}(t) - \mu\mathcal{R}\left(v_{slip,t}\right)\|f_N\|\delta t + \langle F^e_{jt}\rangle \delta t \tag{13}$$

In order to balance the angular momenta, we define a third unit vector $\hat{\mathbf{s}}_{ij} = \hat{\mathbf{n}}_{ij} \times \hat{\mathbf{t}}_{ij}$, to complete a triad. The total angular momentum balance can now be written in terms of components along $\hat{\mathbf{s}}_{ij}$ for the two bodies as follows:

$$I_i\omega_{is}(t+\delta t) = I_i\omega_{is}(t) - R\mu\mathcal{R}\left(v_{slip,t}\right)\|f_N\|\delta t + \langle M_{is}\rangle \delta t \tag{14}$$

$$I_j\omega_{js}(t+\delta t) = I_j\omega_{js}(t) - R\mu\mathcal{R}\left(v_{slip,t}\right)\|f_N\|\delta t + \langle M_{js}\rangle \delta t \tag{15}$$

The derivation of contact interactions presented here is based on the knowledge of restitution coefficient, and the durations of the compression and recovery phases of collision. A physically consistent model for these parameters is therefore necessary to capture the inelastic effects during the collision realistically. We refer to the discussions presented in the classical work by [26] and [43], and for two spheres undergoing elastic collisions, the total contact duration can be shown to be as follows:

$$\delta t = 2.87\left(\frac{m^2}{R v_n E^{*2}}\right)^{1/5} \tag{16}$$

where E^* and R are as defined at the beginning of Section 2.1. The underlying contact forces being completely elastic, the compression and recovery durations should be equal to each other (each being equal to $\delta t/2$ from Eq. (16) above). This is true for low impact velocities, and as the impact velocities increase, inelastic deformations occur more readily, thereby leading to a limiting normal velocity of impact V_{lim} which can be derived from a balance of energies to give the following:

$$\frac{1}{2}mV^2_{lim} = 53\frac{R^3Y^5}{E^{*4}} \tag{17}$$

where Y is the yield stress of the softer of the colliding pair. For any velocity higher than this limit, inelastic deformations occur in the continua of the colliding bodies, and based on the change in energy due to this inelastic deformation, the

restitution coefficient can be derived to be (see [26] for details):

$$e = e(v_{cn}, E^*) = 3.74\sqrt{\frac{Y}{E^*}}\left(\frac{\frac{1}{2}mv_{cn}(t)^2}{YR^3}\right)^{-1/8} \tag{18}$$

The collision durations for the inelastic collision regimes are understandably no longer equally divided, and the compression and recovery durations can be derived as a function of the restitution coefficient as follows:

$$\delta t_1 = \sqrt{\frac{\pi m}{24RY}} \text{ and } \delta t - \delta t_1 = 1.2e\delta t_1 \tag{19}$$

2.2. Particle–surface contact interaction

The contact interactions between a particle and a surface can also be formulated using similar considerations. Assuming the surface description is known to be in form of a mathematical representation $\mathcal{F}(x, y, z) = 0$, it is possible to define a normal vector to the surface by using the following definition (for the unit outward normal) $\hat{\mathbf{n}} = -\frac{\nabla\mathcal{F}}{\|\nabla\mathcal{F}\|}$. We consider a spherical particle approaching this surface, and denote the point of contact with subscript p, and center of mass with the subscript c. If the surface velocity vector is known to be $\mathbf{v}_{surf}$, then the slip velocity at the point of contact can be obtained as:

$$\mathbf{v}_{slip} = \left(\mathbf{v}_p - \mathbf{v}_{surf}\right) - \left[\left(\mathbf{v}_p - \mathbf{v}_{surf}\right)\cdot\hat{\mathbf{n}}\right]\hat{\mathbf{n}} \tag{20}$$

following which, the direction of tangential slip can be defined as:

$$\hat{\mathbf{t}} = \frac{\mathbf{v}_{slip}}{\|\mathbf{v}_{slip}\|} \tag{21}$$

From Fig. 1 the generic form of the contact force acting on the particle can be now motivated to be $\mathbf{F}_{contact} = f_N\hat{\mathbf{n}} - f_T\hat{\mathbf{t}}$. Starting from the balance of linear momentum for the particle over the contact duration and using the definition of restitution coefficient (e) as in the previous section, the final expression for the normal force can be estimated as follows (additional algebra details can be found in Appendix A):

$$\langle f_N\rangle\delta t = \langle f_N\rangle_C\delta t_1 + \langle f_N\rangle_R(\delta t - \delta t_1) = (1+e)\left[mv_{surf,n} - mv_{cn}(t) - \langle F_n^e\rangle\delta t_1\right] \tag{22}$$

Plugging the expression for the total contact impulse into the balance of linear momentum of the particle, the post impact normal velocity of the particle can be obtained as follows:

$$v_{cn}(t+\delta t) = (1+e)v_{surf,n} - ev_{cn}(t) + \frac{1}{m}\langle F_n^e\rangle_R(\delta t - \delta t_1) - \frac{e}{m}\langle F_n^e\rangle_C\delta t_1 \tag{23}$$

The tangential force can be estimated using a regularized friction model analogous to the case of particle contact using Eq. (10). The tangential velocity updates can then be obtained again using Eq. (12), and the updates to the angular velocities due to the contact can be obtained using Eq. (14).

2.3. Particle–fluid interaction

A fully coupled solution of the fluid field incorporating effects of the particle phase on the flow is computationally intensive, and a wide range of existing studies have attempted to tackle such a computation and address underlying issues – for further details see the works by [44–48] amongst others. For applications involving colliding and flowing particulate media, for relatively small particle sizes, the overall dynamics of the ensemble of particles can be approximated reasonably well by assuming that the fluid–particle interactions are one-way coupled (see also the works of [18–21] wherein similar one-way coupled fluid–particle interaction has been employed to study particle motion). Furthermore, for higher density particulate material transported by a gaseous medium, the drag force can be shown to be the most dominant interaction force on the particles. Hence a correct estimate of the drag force is crucial to resolving the dispersed particulate phase behavior. The standard form of the drag force has been used here:

$$\mathbf{F}_{drag} = \frac{1}{2}\rho_f(\pi R_p^2)C_D(Re_p)|\mathbf{u}_f - \mathbf{v}_p|(\mathbf{u}_f - \mathbf{v}_p) \tag{24}$$

where Re_p is the particle slip velocity based Reynold's number given by $Re_p = 2R_p|\mathbf{u}_f - \mathbf{v}_p|/\nu_f$. The drag coefficient C_D can be expressed as a correlation function in terms of Re_p, and the form of the drag coefficient law used in this work has been given by [49] for a broad range of Reynolds number values. The correlation is as below:

$$C_D\left(Re_p\right) = \frac{24}{Re_p}\left(1 + 0.1806Re_p^{0.6459}\right) + \frac{0.4251}{1 + \frac{6880.95}{Re_p}} \tag{25}$$

For the one-way coupled assumption, since the particle-phase does not affect the flow velocity, knowledge of the velocity field is a necessary boundary condition. In order to obtain realistic description of the particulate phase dynamics, a jet velocity profile has been assumed here as follows:

$$u_f = \frac{C_1}{x^{1/3}}\text{sech}^2\left(\frac{C_3 y}{x^{2/3}}\right) \tag{26}$$

$$v_f = \frac{C_2}{x^{2/3}}\left[2\frac{C_3}{x^{2/3}}\text{sech}^2\left(\frac{C_3 y}{x^{2/3}}\right) - \tanh\left(\frac{C_3 y}{x^{2/3}}\right)\right] \tag{27}$$

For three-dimensional simulation, the assumption of axi-symmetry is invoked, and y is replaced by the radial cross-span coordinate location, and x becomes the stream-wise coordinate location. In consistency with free jet-flow from a nozzle, a small region of flow with no entrainment has been assumed near the nozzle exit – which is referred to as the potential core. The form of the velocity ensures that centerline stream-wise velocity decays with distance proportional to $x^{-1/3}$, while entrainment scales as $x^{-2/3}$. Other possible forms of velocity profiles appropriate for spray dynamics have been discussed in detail by [50,14], and [51], and can be imported into the simulation framework easily if required.

3. Adhesion and deposition of particles

The exact mechanism of deposition is a complicated aspect of the governing physics of spray particle deposition technologies. Deposition can result from chemical reactions, solidification of molten droplets, physical bonding, or ionic/electrostatic mechanisms. For a detailed review on these various processes the reader is referred to the work by [1], and the discussions presented by [14]. For the current example, it is sought to have a simple model to treat the basic process of a flowing discrete element sticking to a surface – which can then be hierarchically integrated into a large-scale simulation to understand the global system behavior. To do this, we refer to the macroscopic force of adhesion between a sphere and a surface at very small distances. For two macroscopic particles – themselves composed of a large number of molecules – the net interaction energy between the particles can be computed by summing over all possible interactions between these molecules. Such interactions are characterized by an appropriately modeled interaction potential $U(\mathbf{r})$ – with force $\mathbf{F}_{adh} = -\nabla U$. The general form of this integration can be written as:

$$U_{adh} = \int_{\mathcal{V}_1} d\mathcal{V}_1 \int_{\mathcal{V}_2} d\mathcal{V}_2 \rho_{c1}\rho_{c2} U(\mathbf{r}) \tag{28}$$

where the integrations are done over the volumes $\mathcal{V}_1$ and $\mathcal{V}_2$ of the two bodies with molecule densities ρ_{c1} and ρ_{c2} respectively. The earliest calculations for two rigid spheres using the London Van Der Waals potential form $U(r) = \frac{-C}{r^6}$ was performed by [52], and later modified slightly by [53], and further mathematical details can be found in the extensive discussions presented by [54]. However, particularly for the case of calculating interaction forces and energies between spheres separated by a distance d such that $R_1, R_2 \gg d$, an important result exists due to the work by [55] (see also the discussion in [54] for details). The result, referred to as the *'Derjaguin approximation'*, states that the interaction force between two spheres, for any choice of potential $U(r)$, can be related to the interaction energy between two semi infinite planes as follows:

$$\|\mathbf{F}(d)_{spheres}\| = 2\pi R U(d)_{planes} \tag{29}$$

where R is the effective radius, and for most common potential choices, the integration to obtain $U(d)_{planes}$ is easier to compute than that for spheres. An interesting conclusion that can be drawn from this is the relation between interaction forces and surface energy γ. If we assume that two spheres are in contact, then the actual separation length-scale between the two will be of the order of molecular separation. Representing this separation by ϵ_0, the energy of interaction $U(\epsilon_0) = -2\gamma$, thereby giving:

$$\|\mathbf{F}(\epsilon_0)\| = -4\pi\gamma R \tag{30}$$

The surface energy for creating an interface by bringing two surfaces in contact will be equal to the sum of the original surface energies minus the work down to bring them together. This can be estimated using a simple combination law as follows (see [54] for details):

$$\gamma_{12} = \gamma_1 + \gamma_2 - 2\sqrt{\gamma_1\gamma_2} = \left(\sqrt{\gamma_1} - \sqrt{\gamma_2}\right)^2 \tag{31}$$

Using the Derjaguin Approximation for forces between a sphere and a flat surface, the adhesion force can be written as in terms of the particle–surface interface energy (γ_{12}) as:

$$F^{adh} = -4\pi\gamma_{12} R \tag{32}$$

with $\gamma_{12} \approx 2\sqrt{\gamma_1\gamma_2}$ (if dispersion forces are dominant [54]). Referring to Fig. 2, and using the expression for the final velocity as in Eq. (23), it can be seen that

$$v_{cn}(t+\delta t) = -e v_{cn}(t) + \frac{1}{m}F_n^{adh}(\delta t - \delta t_1) - \frac{e}{m}F_n^{adh}\delta t_1 \tag{33}$$

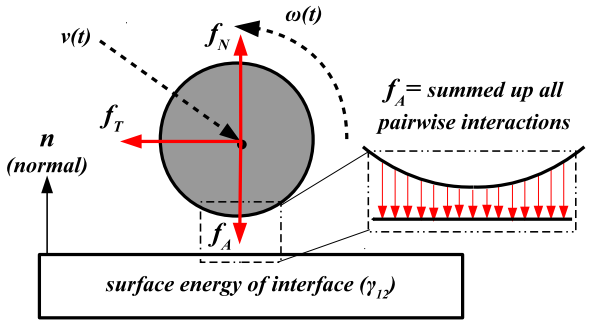

Fig. 2. Schematic for the derivation of a velocity dependent adhesion criteria.

Let us consider $v_{cn}(t) = -v_0$, and $\mathbf{F}^{adh} = -F^{adh}\hat{\mathbf{n}}$, which is consistent with Fig. 2. Furthermore, since the fundamental assumption is that of a nearly-rigid collision, with very small time-scales of collision that do not overlap the simulation time-steps, it will be expected that within one time-step of the simulation, the final velocity $v_{cn}(t+\delta t)$ should be positive if adhesive effects have not dominated the collision. On the other hand, if $v_{cn}(t+\delta t)$ is negative, then the above assumptions are contradicted, and adhesion effects are dominant – and appropriate physical bonding interactions are established. Therefore, if $v_{cn}(t+\delta t) < 0$ it is assumed that the particle sticks to the surface, and assumes the same velocity as the surface. With the further consideration that purely elastic collisions will occur at very low velocities for all practical purposes (which leads to lower collision forces, and more adhesion dominant collisions), it can be assumed that this criteria on final velocity be applied in the regime of inelastic collisions, which then gives us the following final criteria after some algebra:

$$\begin{aligned} 0 &> -ev_0 - \frac{1}{m}F^{adh}(1.2e\delta t_1) + \frac{e}{m}F^{adh}\delta t_1 \\ v_0 &< \frac{0.2F^{adh}\delta t_1}{m} \end{aligned} \tag{34}$$

where we have used the discussions presented in Section 2.1, for the relative magnitude of compression and recovery times in inelastic collision. The adhesion criteria in Eq. (34) will actually lead to very low velocity requirements if the force F^{adh} is computed using the values of surface energy alone. In real applications, however, the effective physical bonding interaction force might be much larger – owing to either the fact that it is trying to represent a different interaction phenomenon, or that the surface to be deposited has been functionally enhanced through some engineered mechanism. Hence the force is multiplied by an appropriate factor α_{ADH} so as to capture the real system behavior more correctly. Thus the velocity dependent criteria becomes $v_0 < 0.2\alpha_{ADH}F^{adh}\delta t_1/m$. Note that as particle size increases, the particle mass increases, thereby leading to very low upper bounds for impact velocities to induce complete adhesion – which is consistent with the physical behavior of such systems. The simple form of Eq. (34) also allows for a simple integration into simulation algorithms, and captures the reported trends on critical velocity and diameter well [56].

4. Simulation framework

4.1. System configuration and boundary conditions

A representative system geometry for the simulation framework has been presented in Fig. 3 where a stream of particles are tracked within a computational domain until it collides with a surface. Depending upon their impact velocity, the

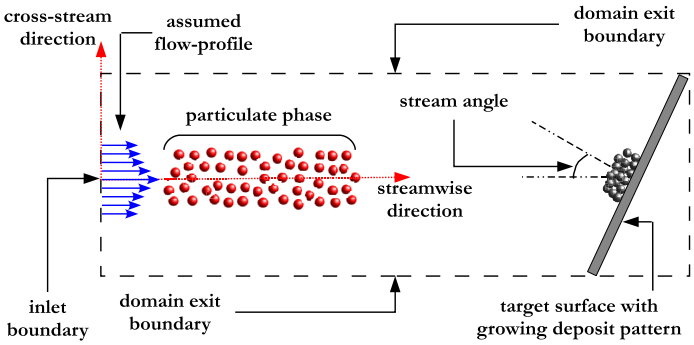

Fig. 3. The schematic representation of the computation domain with identified boundary conditions. Only a cross-section is shown for simplifying the schematic. (For interpretation of the references to color in this figure, the reader is referred to the web version of this article.)

particles either adhere to the surface or collide and bounce back. Apart from the target surface where deposition is being tracked, the computational domain comprises an inlet surface, and boundaries for the overall domain. The latter boundaries are subjected to an *'escape'* boundary condition – that is, any particle crossing this boundary is considered to be exiting the computation domain, and is removed from the calculations. The *'inlet'* boundary condition is modeled in terms of a particle injection. The particle injection is performed by generating random sequentially added spherical particles within a circular cross section area at the inlet boundary. The total number of particles injected N_{in}, and the number of time-steps after which injection is performed T_{in} are set using a desired particle feed-rate (measured in number of particles per second) as follows (where Δt is the numerical time-step):

$$f_{in} = \frac{N_{in}}{T_{in}\Delta t} \tag{35}$$

It is noted here that this is a relatively generic technique of assigning an inlet condition, and can be easily extended to assign a specified momentum or mass flow-rate at the inlet as well.

4.2. Handling particle polydispersity

For the numerical examples illustrated in the subsequent sections, the random variability in the particle sizes was incorporated by assuming the particle sizes to be drawn from an underlain distribution. The most widely used size distribution is based on the Weibull family of distributions (alternatively referred to as the Rosin–Rammler distribution in the literature, see for example [57]). The general form of the distribution is as follows:

$$f(D_p;\lambda,n) = \frac{n}{\lambda}\left(\frac{D_p}{\lambda}\right)^{n-1}\exp\left[-\left(\frac{D_p}{\lambda}\right)^{n}\right] \tag{36}$$

The parameter n is a shape parameter for the distribution function, and is chosen to be a free parameter. For a chosen shape parameter value, the scale parameter λ is then correlated with the median particle size to be simulated using the following relation:

$$D_{median} = \lambda\left[\log(2)\right]^{1/n} \tag{37}$$

The particle diameters are sampled from the distribution in Eq. (36) by using an inverse transform sampling technique.

4.3. Numerical formulation

The particle-level physical interaction models described in Sections 2 and 3 can now be hierarchically assembled to construct an overall simulation framework for the particulate spray dynamics. Considering an ensemble of N particles $\mathcal{P}_N$ as shown in Fig. 3, the individual motion equations can be written for each particle (marked in red) as follows:

$$\frac{d\mathbf{v}}{dt} = \frac{1}{m_i}\left[\mathbf{F}_i^{fl} + \mathcal{I}_s\left(\mathcal{P}_i,\mathcal{S}\right)\left[\mathbf{F}_i^{adh} + \mathbf{F}_i^{c}\left(\mathcal{P}_i,\mathcal{S}\right)\right] + \sum \mathcal{I}_p\left(\mathcal{P}_i,\mathcal{P}_j\right)\mathbf{F}_{ij}^{c}\right] \tag{38}$$

$$\frac{d\mathbf{x}_i}{dt} = \mathbf{v}_i \tag{39}$$

where $\mathcal{I}_s$ and $\mathcal{I}_p$ are indicator functions for particle–surface and particle–particle collisions respectively. For the derived forces from a global momentum balance formulation presented in Section 2, the forms of these indicator functions for a pair of particles can be mathematically defined as:

$$\begin{aligned}\delta_n &= \|\mathbf{r}_i - \mathbf{r}_j\| - \left(R_i + R_j\right)\\ \mathcal{I}_p(i,j) &= \begin{cases} 1 & \text{if } \delta_n \le 0 \text{ and } v_{ij,n} < 0 \text{ (contact)}\\ 0 & \text{if } \delta_n > 0 \text{ or } v_{ij,n} > 0 \text{ (no contact)}\end{cases}\end{aligned} \tag{40}$$

For a particle–surface contact check, the form of the indicator function remains the same. The only variation is in the evaluation of the contact overlap δ_n. For interactions between a spherical particle and a plane surface – which is the application we are interested in here – this can be estimated by considering the plane to be defined as $ax + by + cz + d = 0$ in three-dimensional Euclidean space, and writing the overlap using the total distance of the center of the sphere from this plane as follows:

$$\begin{aligned}\delta_n &= \frac{\|a_j x_i + b_j y_i + c_j z_i + d_j\|}{\sqrt{a_j^2 + b_j^2 + c_j^2}} - R_i\\ \mathcal{I}_s(i,\mathcal{S}_j) &= \begin{cases} 1 & \text{if } \delta_n \le 0 \text{ (contact)}\\ 0 & \text{if } \delta_n > 0 \text{ (no contact)}\end{cases}\end{aligned} \tag{41}$$

The check on the relative velocities for the contacting particles in Eq. (40) is critical to resolve the contact forces accurately. The evaluation of the collision indicator $\mathcal{I}_p$ is the most computationally intensive step – since it requires a pairwise collision check for all N particles in the ensemble. However, potential collisions can only occur amongst the nearest neighbors provided the time-steps are not erroneously big. Therefore appropriate binning and neighbor-list construction algorithms can be employed to resolve the geometrical locality of the particle ensembles and perform contact checks only amongst the close neighbors for a particle. A wide variety of such algorithms exist (see for example, the works by [22,58] (specifically Chapter 7), [59,60], the classical work by [61], more recent works of [62,63] (for more algorithmic details), and [64]). Implementation of such algorithms reduce significantly the time-complexity of resolving the collision physics. For the simulation framework presented here, a direct binning algorithm is used. The domain is decomposed into rectangular bins, and for each particle, contact checks are performed with particles in its own bin and in all the neighboring bins. The bin size is set based on a scaling with respect to the largest particle diameters in the generated particle ensemble, and detailed algorithmic analysis is presented in [22].

4.4. Solving the system equations

Within a certain time-step, physical contact for a particle or a surface may happen at any instant. However, checking for contacts inside of a time-step will be a computationally intensive task. Hence as an approximation, it can be assumed that the instant when contact occurs is shifted to the beginning of the time-step. This is analogous to the 'Collide-and-Stream' type calculations typical in Lattice–Boltzmann type simulations (see [65], and more specifically [37], and [25] for such calculations in particulate flow problems). This means that for an individual particle, contacts with another particle or a surface at a time instant $t^* > t_n$ are resolved by applying the appropriate force at the beginning of the time-step t_{n+1}. The motion equations for each individual particle are solved using a one-step ϕ discretization scheme outlined as follows:

$$\mathbf{v}_i^{N+1} = \mathbf{v}_i^N + \frac{\Delta t}{m_i}\left[\phi \mathbf{F}_{i,net}^{N+1} + (1-\phi)\mathbf{F}_{i,net}^N\right] \tag{42}$$

$$\mathbf{x}_i^{N+1} = \mathbf{x}_i^N + \Delta t\left[\phi \mathbf{v}_i^{N+1} + (1-\phi)\mathbf{v}_i^N\right] \tag{43}$$

$$\mathbf{F}_{i,net}^N = \mathbf{F}_i^{fl,N} + \mathcal{I}_s\left(\mathcal{P}_i^N, \mathcal{S}\right)\left[\mathbf{F}_i^{adh,N} + \mathbf{F}_i^{c,N}\left(\mathcal{P}_i^N, \mathcal{S}\right)\right] + \sum \mathcal{I}_p\left(\mathcal{P}_i^N, \mathcal{P}_j^N\right)\mathbf{F}_{ij}^{c,N} \tag{44}$$

where superscripts N and $N+1$ indicates the indices of the current and the future time-step in the discretization respectively. The notation $\mathcal{P}_i^N$ indicates the dynamic phase-space location of the i'th particle at the time-step indexed by N. This is a generalized one-step scheme, with $\phi \in [0,1]$, and $\phi = 0$ is the explicit Euler integration scheme, while $\phi = 1$ is the fully implicit Euler integration scheme. The implicit implementation of the position and velocity updates, as is evident from Eqs. (42) and (43), requires an iterative solution for $\mathbf{v}_i^{N+1}$ and $\mathbf{x}_i^{N+1}$. A fixed-point iterative scheme can be formulated by re-arranging Eq. (42) and Eq. (43) as follows (see [66], and [67] for details):

$$\mathbf{v}_i^{N+1} = \mathcal{G}_v\left(\mathbf{v}_i^{N+1}; \mathcal{P}_i^{N+1}, i = 1, \ldots, N_p\right) + \mathcal{R}_v \tag{45}$$

$$\mathbf{x}_i^{N+1} = \mathcal{G}_x\left(\mathbf{x}_i^{N+1}; \mathcal{P}_i^{N+1}, i = 1, \ldots, N_p\right) + \mathcal{R}_x \tag{46}$$

$$\mathcal{G}_v = \frac{\Delta t}{m_i}\phi \mathbf{F}_{i,net}^{N+1} \tag{47}$$

$$\mathcal{R}_v = \mathbf{v}_i^N + \frac{\Delta t}{m_i}(1-\phi)\,\mathbf{F}_{i,net}^N \tag{48}$$

$$\mathcal{G}_x = \Delta t \phi \mathbf{v}_i^{N+1} \tag{49}$$

$$\mathcal{R}_x = \mathbf{x}_i^N + \Delta t\,(1-\phi)\,\mathbf{v}_i^N \tag{50}$$

where an explicit dependence of the forces (and therefore the functions $\mathcal{G}_v$ and $\mathcal{G}_x$) on the overall phase-space of the particles has been indicated by the additional function argument $\mathcal{P}_i^{N+1}$. The iterations can now be carried out as follows:

$$\mathbf{v}_i^{N+1,K+1} = \mathcal{G}_v\left(\mathbf{v}_i^{N+1,K}; \mathcal{P}_i^{N+1}, i = 1, \ldots, N_p\right) + \mathcal{R}_v \tag{51}$$

$$\mathbf{x}_i^{N+1,K+1} = \mathcal{G}_x\left(\mathbf{x}_i^{N+1,K}; \mathcal{P}_i^{N+1}, i = 1, \ldots, N_p\right) + \mathcal{R}_x \tag{52}$$

where the superscript K indicates the number of iterations. The successive fixed-point iterations are carried out until the total particle phase space error is below a certain specified threshold value. The form of the error function has been presented below:

$$e_{total} = \sum_i \frac{\|\mathbf{v}_i^{N+1,K+1} - \mathbf{v}_i^{N+1,K}\| + \|\mathbf{x}_i^{N+1,K+1} - \mathbf{x}_i^{N+1,K}\|}{\|\mathbf{v}_i^{N+1,K+1} - \mathbf{v}_i^{N+1,0}\| + \|\mathbf{x}_i^{N+1,K+1} - \mathbf{x}_i^{N+1,0}\|} \tag{53}$$

Algorithm 1 The procedural implementation of the simulation framework. The evaluation of the contact, fluid, and adhesion forces, and resolution of particle adhesion vs rebound is using the models described in Sections 2 and 3.

instantiate and initialize all data structures
construct the binned neighbor-list
set-up fluid velocity profile
$\Delta t \leftarrow$ time-step size; $T_{sim} \leftarrow$ simulation-time
for $(t \leq \text{mod}(T_{sim}/\Delta t))$ **do**
  if $(\text{mod}(t/T_{in}) = 0)$ **then**
    inject N_{in} particles
  end if
  while $(e_{total} \leq e_{TOL})$ **do**
    $\mathbf{F}^c_{ij} \leftarrow$ build all contact forces using binning $\forall i, j = 1, \cdots, N_p$
    $\mathbf{F}^{fl}_i \leftarrow$ build all fluid forces $\forall i = 1, \cdots, N_p$
    resolve all adhesions at the surface $\forall i = 1, \cdots, N_p$
    if (particle i is not deposited) **then**
      particle rebounds with $\mathbf{F}^c_i \leftarrow$ contact force between particle and surface
    end if
    calculate total force as sum of all forces
    for *particle_index* $= 1$, *num_particles* **do**
      update velocities
      update positions ▷ as from Eqs. (42), (43), (44)
    end for
    $e_{total} = \sum_i \frac{\|\mathbf{v}_i^{N+1,K+1} - \mathbf{v}_i^{N+1,K}\| + \|\mathbf{x}_i^{N+1,K+1} - \mathbf{x}_i^{N+1,K}\|}{\|\mathbf{v}_i^{N+1,K+1} - \mathbf{v}_i^{N+1,0}\| + \|\mathbf{x}_i^{N+1,K+1} - \mathbf{x}_i^{N+1,0}\|}$
  end while
  reset the particle bins
  conditionally dump particle phase-space data to external file for post-processing
end for

Table 1
Representative simulation parameters used for the numerical experiments performed in this study.

Parameter	Values/ranges used
Target material properties	80.0 GPa (shear), 160.0 GPa (bulk)
Particle material properties	77.0 GPa (shear), 167.0 GPa (bulk)
Target material yield strength	690.0 MPa
Particle density	5680.0 kg/m^3
Surface energy of target surface	1100.0e–3
Surface energy of particles	46e–3 J/m^2
Friction coefficient	0.50–0.60 (variable)
Friction regularization parameter	0.0001
Restitution coefficient	0.80 (variable based on velocity)
Carrier fluid density	1.10 kg/m^3
Carrier fluid viscosity	25.0e–6 m^2/s
Release nozzle radius	0.01 m
Target surface stand-off distance	0.30 m
Simulation time-step (Δt)	2×10^{-6}–5×10^{-6} s

where superscripts $N+1, 0$ indicate the initial guesses for the positions and velocities at the beginning of the time-step to get the iterative calculations started. The overall implementation of the solution algorithm has been presented in form of a pseudocode in Algorithm 1.

5. Numerical example

5.1. Three-dimensional simulation of particle flow and deposition

Fully three-dimensional particle flow and deposition simulations were performed, with varying system parameters. The global system parameter values and ranges have been presented in Table 1. Particles were released at the rate of 50 particles per time step (N_{in}) after every 100 time-steps (T_{in}), and particle motion equations were solved using a trapezoidal integration scheme (that is, $\phi = 0.5$ in Eqs. (42), and (43)). These parameter choices are reasonable, and have been kept constant across a broad range of numerical experiments with the developed simulation framework. The various forms of particle size distributions used in the numerical experiments have been presented in Fig. 4.

An illustration of the dynamics of the particle stream dispersed in the carrier fluid and being propagated towards the target surface is presented in form of snapshots in Fig. 5. The particles are released with an inlet velocity that has been chosen uniformly randomly between 0 and 50 m/s. Owing to the randomness in particle size, and in particle release velocities, and also the response of the particles to the entrainment velocity in the carrier fluid flow field, the particles undergo mid-air collisions as they propagate towards the target surface. These collisions cause a scatter in the particle deposit pat-

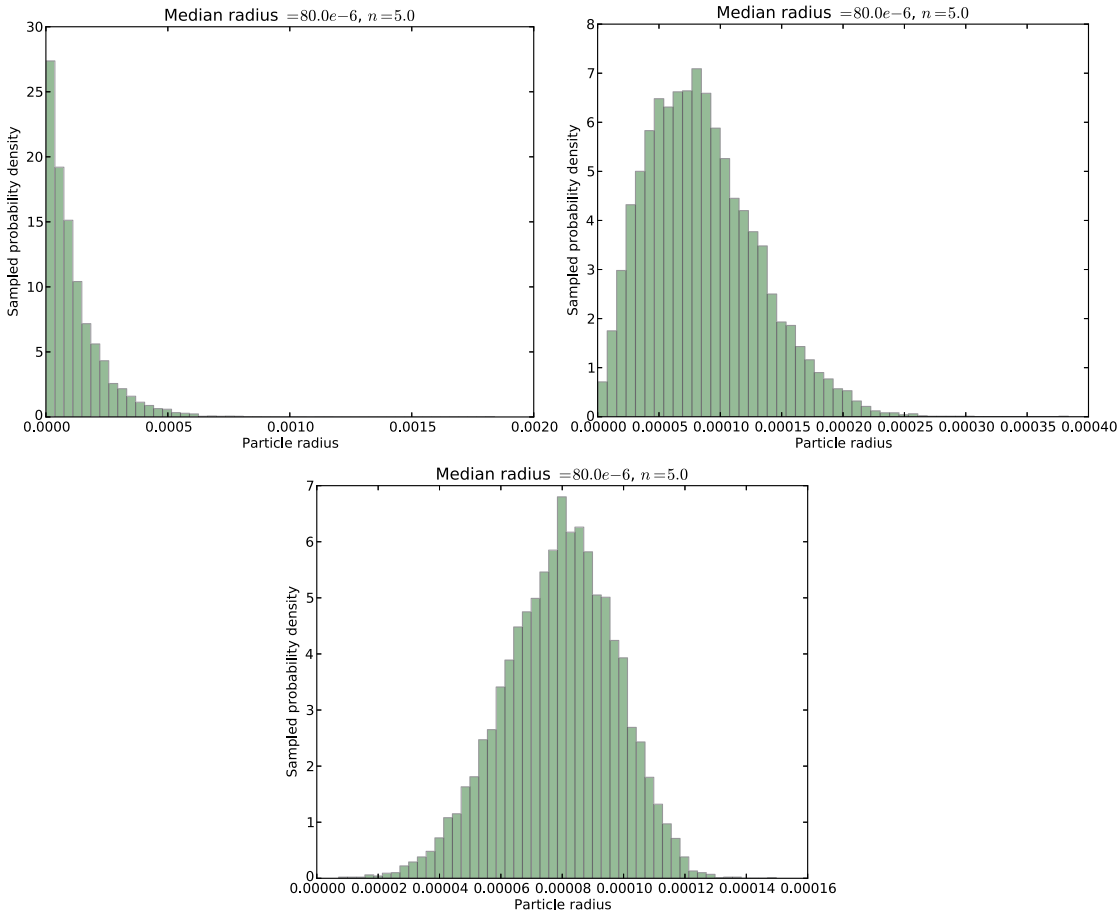

Fig. 4. The particle size distributions used in the numerical experiments presented here.

tern on the target surface. Also, owing to the variability in the particle impact velocities, based on the deposition criteria, a proportion of incoming particles collide and bounce back instead of getting deposited. Since the particle response to the imposed flow velocity field varies proportionally to the square of particle diameter, variabilities in particle size will lead to variabilities in the particle velocities in the carrier fluid. Additionally, the nature of the imposed flow is such that particles close to the spray centerline travel faster, and there is an entrainment flow radially inwards into the spray. Smaller particles in the spray respond to this entrainment sooner, and attain a cross-span velocity component. These factors contribute to increased number of inter-particle collisions. A typical deposit pattern produced from such a process, and its microstructure have been illustrated in Fig. 6, where the same particle spray process was allowed to evolve for a longer duration until a sum total of 50 050 particles were injected into the plume. Due to the particle collisions as mentioned earlier, the deposit pattern shows significant levels of scatter – most of which have been zoomed out of in Fig. 6. In order to compare the uniformity of the deposit pattern and the scatter produced on the target surface, a set of deposit pattern data have been visualized for various different simulation configurations in Fig. 10, a detailed discussion on which will be presented in the following subsection.

5.2. Analysis and parameter variations

Further analysis of the overall trends in the deposition process is now motivated in terms of simple metrics relating to the deposit pattern which are obtained from post-processing the deposited particles and their spread on the target surface. The following metrics have been defined and used as a part of this study:

- deposit fraction $= \frac{N_{del}}{N_{inj}}$, where N_{del} is the number of deposited particles,and N_{inj} is the number of injected particles, both measured after a fixed simulation time interval
- volume fraction $= \frac{\sum \mathcal{V}_p}{\mathcal{V}_{target}}$, where $\mathcal{V}_p$ indicates volume of a deposited particle lying within a chosen deposit-target region, and $\mathcal{V}_{target}$ indicates the total volume of the deposit-target (e.g. for our simulations it is the circular pellet of width 0.01 m)

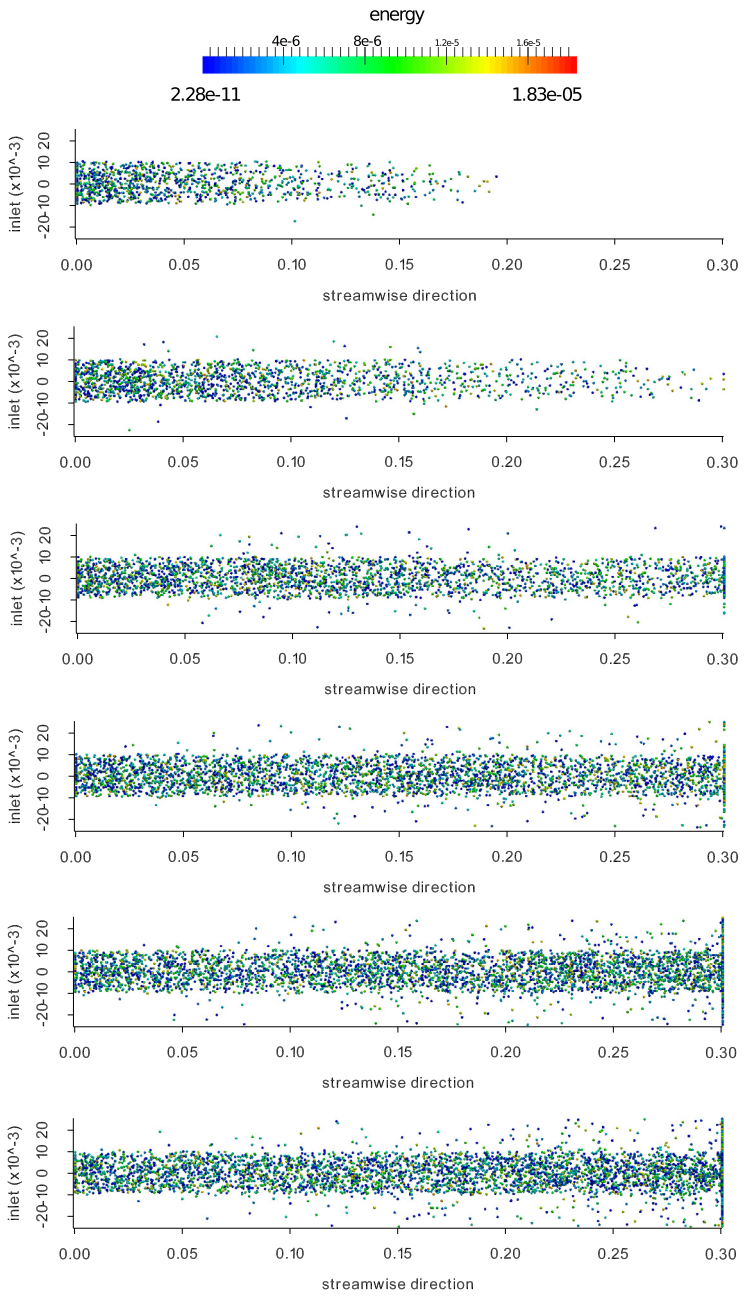

Fig. 5. Successive snapshots of a three dimensional particle stream of mono-disperse particles impacting a target surface with a deposit factor of 5000. (Particle markers made slightly bigger to aid better visualization). (For interpretation of the colors in this figure, the reader is referred to the web version of this article.)

- mean spread $\mu = \frac{\sum |\mathbf{x}_p - \mathbf{x}_0|}{N_{dep}}$
- scatter in spread $\sigma = \sqrt{\frac{\sum \left(|\mathbf{x}_p - \mathbf{x}_0| - \mu\right)^2}{N_{dep}}}$
- maximum deposit thickness $h = \max(\mathbf{x}_i \cdot \mathbf{s}) - \min(\mathbf{x}_i \cdot \mathbf{s})$ where $\mathbf{s}$ is the vector along the streamwise direction of spray plume

In order to isolate the effect of variations in the deposition parameter α_{ADH} and its relation to the characteristic release velocity, spray particles sampled from a distribution with mean radius 80 μm and shape parameter $n = 5.0$, were directed towards a target surface with varying levels of α_{ADH} for stream velocities of 30.0 m/s, 50.0 m/s, and 80.0 m/s respectively. The variations in the deposit volume fraction, the measure of maximum deposit thickness, the mean deposit spread, and

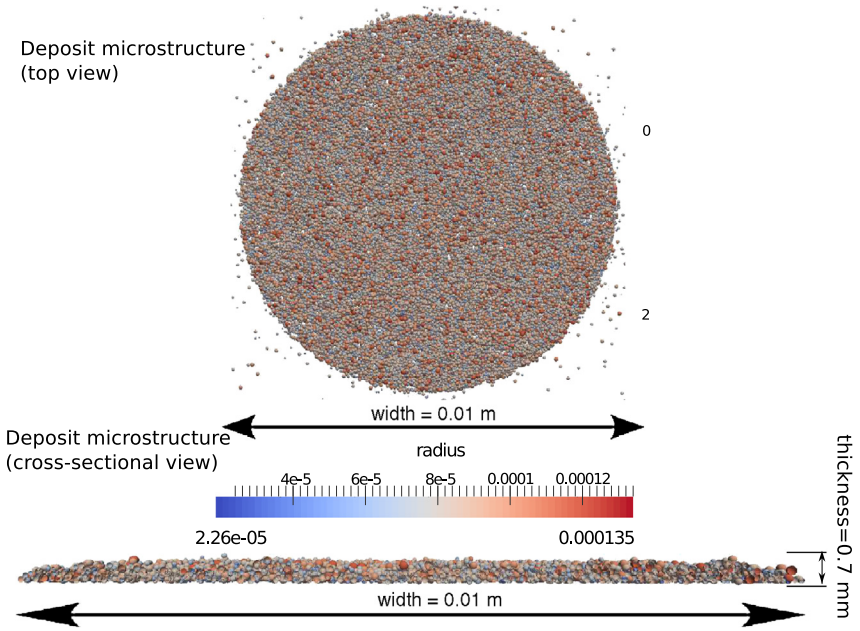

Fig. 6. Illustration of a representative deposit microstructure obtained after 50 050 particle injections were completed, for a median particle radius of 80.0 μm. (For interpretation of the colors in this figure, the reader is referred to the web version of this article.)

the standard deviation have been compared in Fig. 7. The metric for the deposit depth has been normalized using the median particle radius used in the simulations. It is observed, in consistency with the velocity dependent deposition criteria implemented in the simulations, that lower particle impact velocities lead to higher probabilities of deposition. However, as is evident from an analysis of the particle trajectories, slower particle release velocities also cause a higher number density in the stream and lead to higher rate of inter-particle collisions, causing a higher scatter in the deposit pattern (higher standard deviation in Fig. 7 (bottom, right)). These competing phenomena therefore also explain the observation that volume fraction is consistently higher for the more moderate velocity in Fig. 7 (top, left). This particular aspect is further illustrated in Fig. 8, where particle trajectories for varying characteristic release velocities have been presented with a clear indication of more scatter due to collisions for the slower release velocity simulation (top).

Variability in particle sizes also plays an important role in the overall system dynamics. While poly-dispersity of particle sizes will lead to lesser collisional cross-sectional area, the corresponding particle Stokes numbers become variable, and lead to higher occurrence probability for collision. Furthermore, since the response of a particle to the imposed fluid flow will additionally be dependent on the initial velocity of release, variabilities in the release velocity can affect the probability of occurrence of inter-particle collision, and scatter in the deposition patterns. A comparison of these effects, in combination with the variation in deposit parameter α_{ADH}, has been presented in Fig. 9 (top-left), where the total deposit fraction after a fixed duration of simulation time have been compared for various combinations of the aforementioned factors. The trends in Fig. 9 (top-left) can be explained by considering the combined effect of the velocity threshold for deposition for a given α_{ADH} (Eq. (34)), and the total number of particles being dynamically transported to the target surface. For a given velocity, the deposit fraction varies rapidly to start with, and gets flatter as α_{ADH} increases. Thus for a chosen particle velocity regime, deposit fraction varies slowly for values of α_{ADH} much higher than the threshold, and rapidly for α_{ADH} much lower than the threshold. For Fig. 9 (top-right), the combined effect of reduced collisional cross-section and increased variability in Stokes numbers as mentioned above is manifested in the trends. The trend in Fig. 9 (middle-left) is due to the fact that variabilities in the particle response to the fluid flow causes more collisions and lesser particles to be transported to the target surface within a fixed simulation duration.

The rate at which the deposit pattern grows in number can also be tracked with respect to simulation time, and provides an additional metric to probe and understand the trends in the system behavior. To illustrate the same, two different sets of simulation data have been presented in Fig. 9 on the middle-right, and bottom-left panels. For a fixed characteristic stream velocity of 50.0 m/s, and particles of median radius 80.0 μm sampled from a distribution with $n = 5$, the deposit rates have been post-processed for varying choices of the deposit parameter α_{ADH}. The time-variation of the total number of deposited particles, have been presented in Fig. 9 on the bottom-left panel. The corresponding rates have been calculated as the slopes of the last few time-steps when the deposition and rebound process nearly attains a quasi-steady state, and have been presented on the bottom-right panel. The large variation at a specific regime of deposit parameter values is characteristic of the threshold for the velocity regime for the particular spray particle dynamics in consideration. The trend for the time-variation of the total number of deposited particles with respect to particle distribution shape parameter as presented in Fig. 9 on the middle-right panel, is a little more indirect, and can be rationalized by comparing the corresponding

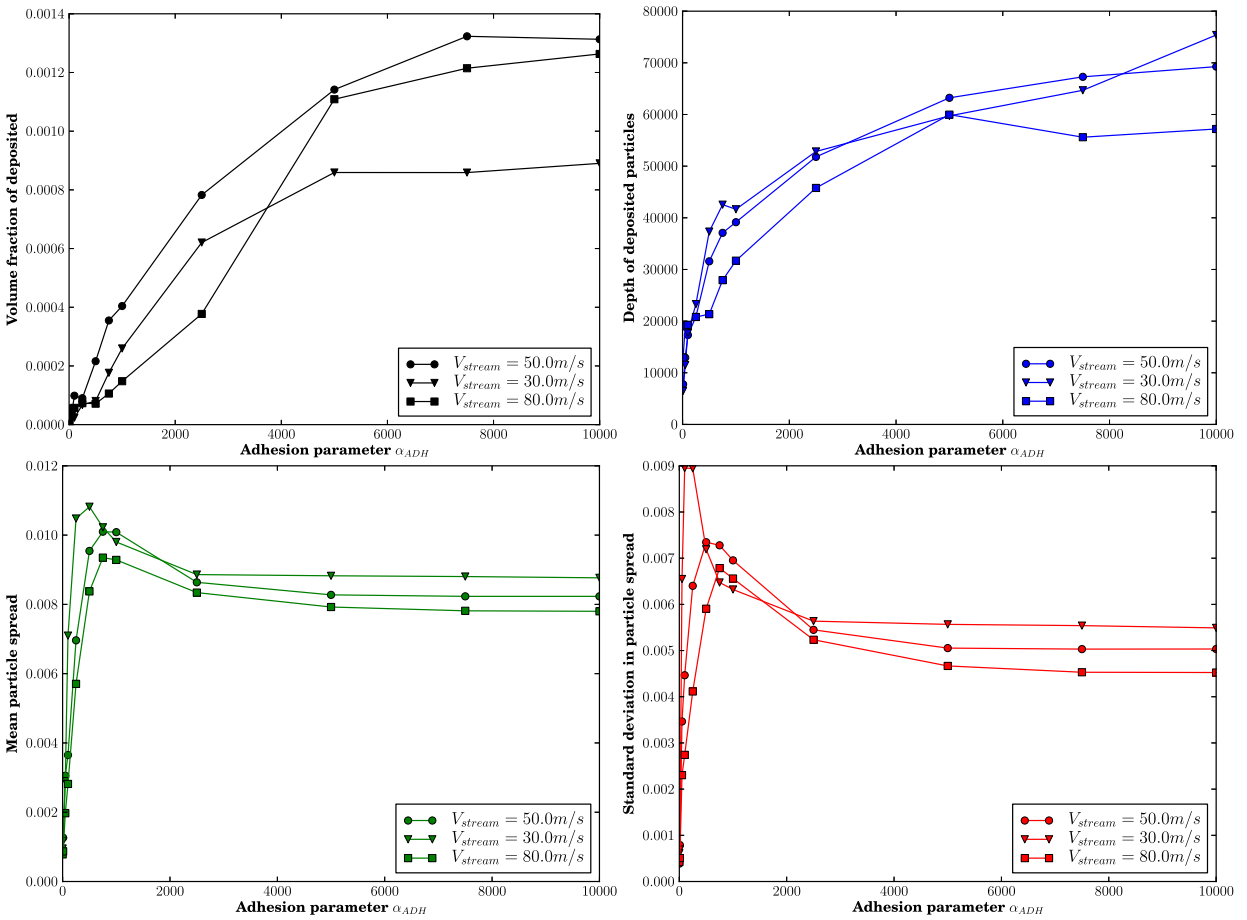

Fig. 7. Comparison of deposit metrics with variations in the deposit parameter and carrier stream velocity. Clockwise from top left: variations in volume fraction, measure of deposit height (in proportion of median particle radius), standard deviation, and mean value of the deposit spread distance.

distribution functions presented in Fig. 4. It is evident that as n varies from 1 to 5, the sampled particle radius values are more evenly spread around the median radius value of 80.0 μm. This causes the dynamic behavior of the polydisperse particle sprays to resemble that of the monodisperse spray for increased n. Physically, the slopes of these time-varying count of deposited particles are a resultant of the velocities attained by the particle owing to the fluid–particle interactions and particle–particle collisions, and the mechanism of deposition that causes a fraction of the incident particles to bounce back depending upon their velocity prior to impact. A direct visualization of the combined effect of these phenomena on the deposit pattern microstructure is also illustrated in form of a series of deposit pattern snapshots in Fig. 10. Clearly, for lower deposition factors, the higher release velocities lead to higher particle velocities causing more rebounding particles (deposit pattern on top-right). However, for higher deposit factor, the higher release velocities cause lesser in-flight collisions between particles – leading to deposit pattern becoming more uniform as we increase release velocities (from bottom-left to bottom-right).

6. Concluding remarks

In the present study, a three dimensional discrete element framework has been presented for particle spray deposition processes. The framework encompasses particle–particle collisional interactions, one-way fluid–particle interactions, particle–surface contact interactions, and a model for particle deposition upon impact on a flat target surface. The latter has been derived from a balance between near-field physical bonding interactions and forces due to mechanical contact. This criteria has been augmented using a factor α_{ADH} that models the extent by which the actual bonding mechanisms differ from that of near-field surface interactions. The derived criteria actually captures the relation between critical velocity and particle diameter as reported through experiments in the literature (see [56] for example). Detailed numerical examples have been presented to illustrate and analyze not only the dynamics of the particle streams due to the combined multi-physical interactions, but also the deposit patterns obtained. Numerical experiments on parameter variations were also performed using the framework to investigate the effect of in-flight dynamics and collisions on the nature of the deposit pattern obtained. It was observed that owing to the particle injection strategy described in Eq. (35), slower particle injection

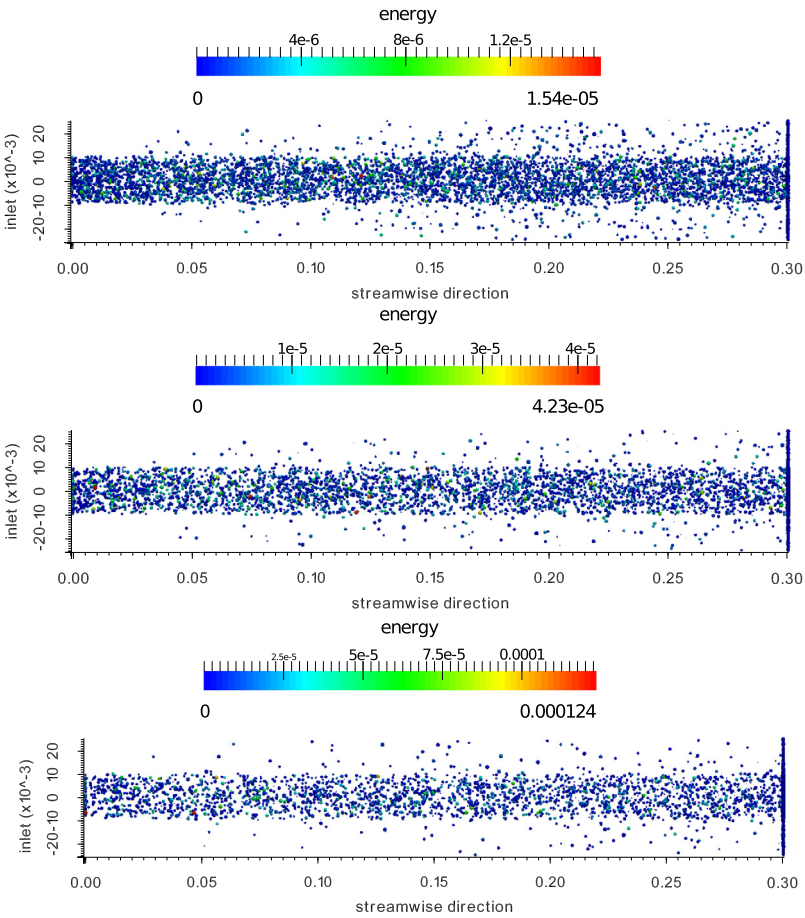

Fig. 8. Snapshots of fully developed particle spray dynamics for characteristic release velocities 30.0, 50.0 and 80.0 m/s from top to bottom, showing the varying extents of particle scatter due to inter-particle collisions. (For interpretation of the colors in this figure, the reader is referred to the web version of this article.)

velocities or slower nozzle gas velocities cause an increase in particle number density in the spray plume. From a kinetic theory perspective, an increase in the number density of particles in a region in space will increase the frequency of particle collisions – thereby leading to increased scatter in the deposit. However, amongst the range of particle incidence velocities during impact with the target surface, lower velocities should lead to more probability of deposition. The overall deposit pattern microstructure is governed by the competition between these two factors. It was also observed that deposit number fraction and volume fraction vary rapidly at regimes of α_{ADH} lower than the threshold regime, and slowly at regimes of α_{ADH} higher than the threshold for a chosen stream velocity. Effects of particle size polydispersity on deposition rates and deposit properties were also discussed. The dependence of the deposit patterns and their properties on in-flight collisions amongst traveling particles would have been impossible to understand with any continuum based approaches.

It is to be noted that effect of the swirling fluid velocities at locations very close to the target surface owing to fluid stagnation has not been incorporated in this analysis, and neither have turbulent fluctuations in the velocity field. For the former, however, we must realize that the nature of the flow field is such that it decays with stand-off distance from the nozzle, causing flow velocities close to target surface to be substantially lower. At such flow velocities, considering the high ratio of particle density to carrier gas density and the highly inertial motion of the particles, it is expected that any variations in the flow field will only change locally the trajectories of already accelerated particles, affecting the local distribution of distributed particles but not changing the global properties and their qualitative trends as presented here. As for turbulence, additional fluid velocity fluctuations in the carrier flow field will only cause added particle velocity variabilities and potentially lead to higher collision probabilities, and greater extent of scatter in deposit pattern. The discussions presented here therefore form a good baseline estimate of the qualitative trends for such processes. Furthermore, implicit with the one-way coupled assumption, is the flexibility of incorporating additional velocity field fluctuations due to turbulence quite easily into the framework, and possible approaches for this have been presented by [68] amongst others. We also remark that for all the simulations discussed here the particle number densities were maintained in the regime where the assumption of collisionally driven, one-way coupled particle flow was still valid. This was achieved by controlling the parameters

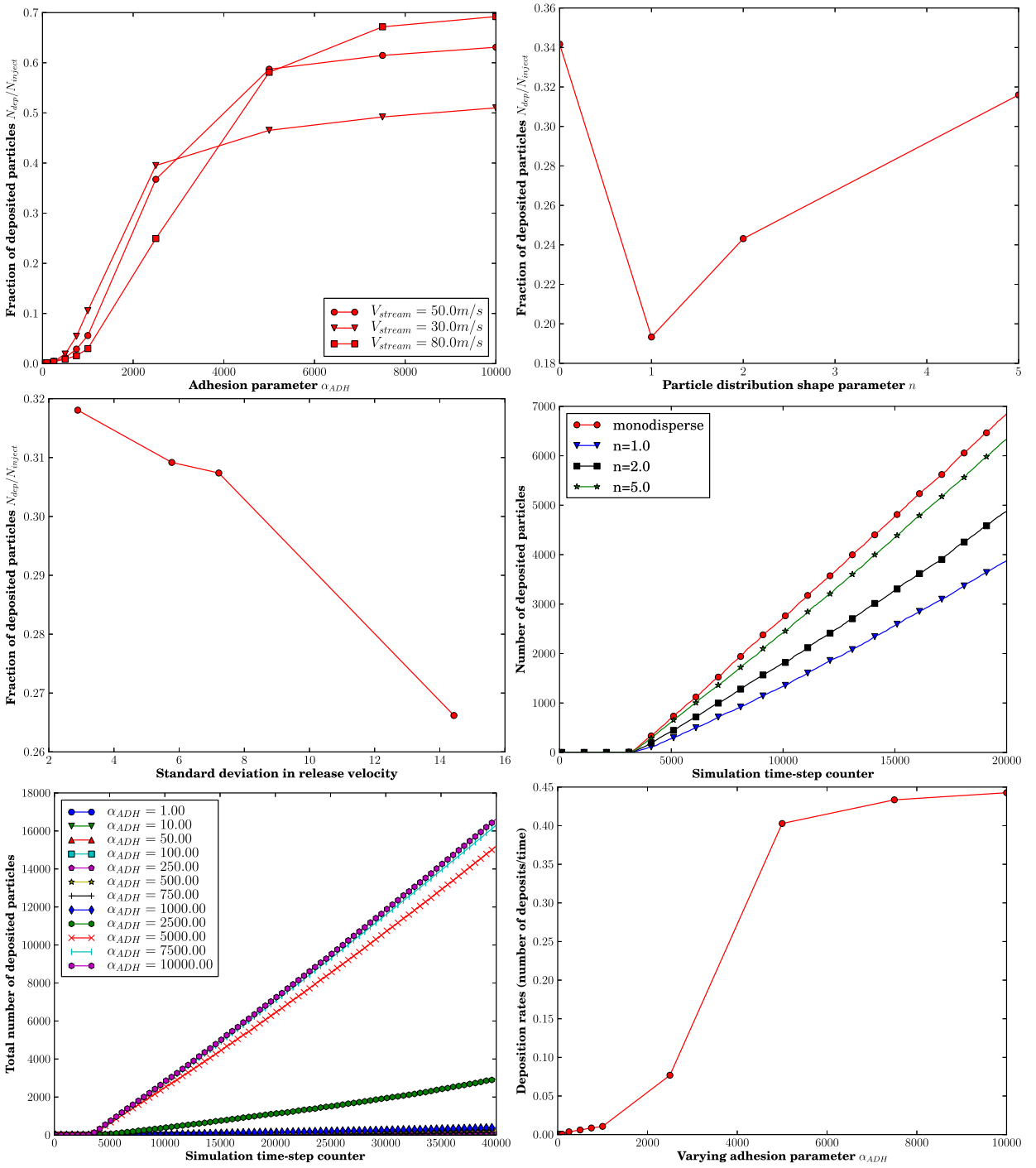

Fig. 9. Effect of parameter variations on deposit number fraction and deposit growth rate. The successive subfigures are enlisted as follows – variation of the fraction of injected particles deposited with changes in deposit parameter and carrier stream velocity is on top-left, with particle size distribution on top-right, and with variance in particle injection velocities on middle-left. Time-variation of the number of deposited particles for varying particle size polydispersity is on middle-right, and with varying deposit parameter is on bottom-right. Finally the rate of growth of deposit is measured for varying deposit parameters is on bottom-left.

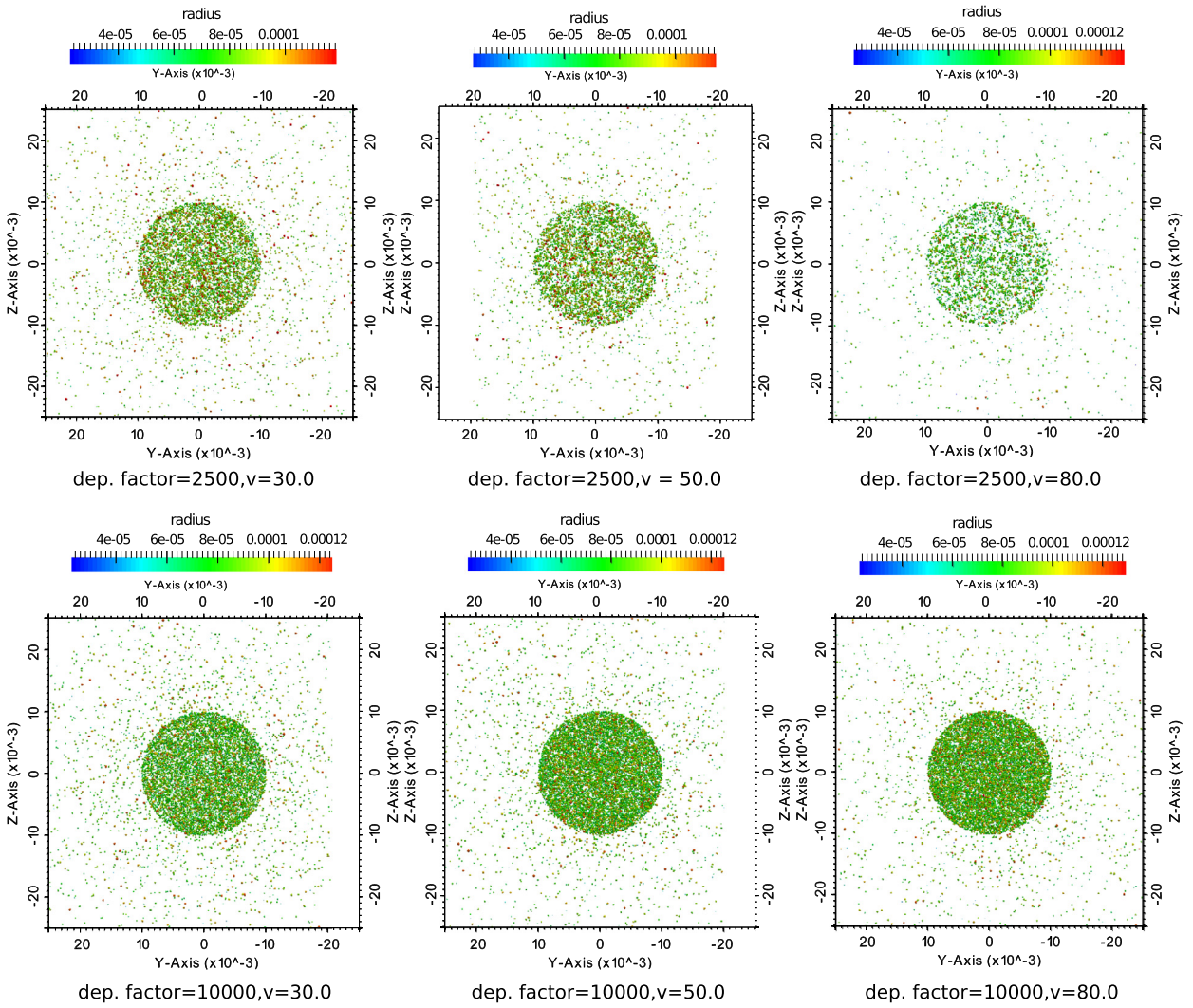

Fig. 10. Comparison of deposit pattern microstructures (top view) for varying deposit parameters, and varying carrier fluid stream velocities. The observations are consistent with the trends in Fig. 7. (For interpretation of the colors in this figure, the reader is referred to the web version of this article.)

in Eq. (35). Further considerations of including turbulent flow field, and resolving two-way, particle–fluid coupling are areas of active investigation by the authors.

It is also noted that considerations for calculating an appropriate value for the deposit parameter α_{ADH} for specific applications have not been discussed here. This model parameter estimation will only be possible by performing appropriate experimentation, and using the experimental data to construct corresponding inverse problems. We remark that experiments based on Atomic Force Microscopy for individual particles as illustrated in [69], amongst others, could be utilized to set-up a procedure for estimating this parameter, and used in simulations thereafter. The specific aspect of validation of numerical simulations is also worth a mention. While extensive validation tests have not been undertaken as a part of this work, some comments can be made about possible strategies to validate the overall framework. Individual particle contact model parameters can be estimated, and their overall motion under the influence of collisional interactions can be validated using inverse problems based on available experimental data, as illustrated in [70] and [71] for different applications. The specific issue of adhesion can be validated again using experiments as mentioned above [69,72]. This aspect of parameter estimation, and validation using inverse problem formulation however deserves a more detailed discussion by itself, and is currently being investigated by the authors. Additionally, the bonding and deposition criteria derived here is based on physical bonds being established depending on the particle kinetic energy. Hence an upper threshold on impact velocities is obtained. Alternatively, for processes involving a transformation of kinetic energy into plastic deformation this trend should be reversed. This is characteristic of cold-spray deposition processes (see [73], and [8]) – where the critical velocity is such that velocities lower than critical are ineffective in causing bonding through deformation (see the discussion

in [74]). The framework developed here is general enough to be able to incorporate such criteria as well, thereby rendering a substantially broad applicability to the discussions presented here.

Acknowledgements

The authors would like to acknowledge the financial support provided by Siemens Energy through the "*Center of Knowledge Interchange*" (CKI) program at University of California, Berkeley, and the support provided through the ongoing collaboration between King Abdullah University of Science and Technology (KAUST), and University of California, Berkeley.

Appendix A. Contact force derivation

For the sake of completeness, we present here the algebraic manipulations involved in the derivation of the contact force expressions in Eqs. (7) and (22). We start from the pairwise balance of linear and angular momenta (re-written here from Eqs. (5), and (6)),

$$m_i \mathbf{v}_i(t+\delta t) - m_i \mathbf{v}_i(t) = \int_t^{t+\delta t} \left[\mathbf{F}_i^c + \mathbf{F}_i^e\right] dt = \langle \mathbf{F}_i^c \rangle \delta t + \langle \mathbf{F}_i^e \rangle \delta t, \tag{a}$$

$$m_j \mathbf{v}_j(t+\delta t) - m_j \mathbf{v}_j(t) = \int_t^{t+\delta t} \left[\mathbf{F}_j^c + \mathbf{F}_j^e\right] dt = \langle \mathbf{F}_j^c \rangle \delta t + \langle \mathbf{F}_j^e \rangle \delta t. \tag{b}$$

As mentioned in Section 2.1, assuming the contact force is represented as $\mathbf{F}_i^c = f_N \hat{\mathbf{n}}_{ij} + f_T \hat{\mathbf{t}}_{ij}$, and taking a dot-product of Eq. (a) and (b), with $\hat{\mathbf{n}}_{ij}$, we get

$$m_i v_{in}(t+\delta t) - m_i v_{in}(t) = \langle f_N \rangle \delta t + \langle F_{in}^e \rangle \delta t, \tag{c}$$

$$m_j v_{jn}(t+\delta t) - m_j v_{jn}(t) = \langle -f_N \rangle \delta t + \langle F_{jn}^e \rangle \delta t. \tag{d}$$

The collision linear momentum balance can further be decomposed into a balance over the 'compression' and the 'recovery' phase of the collision:

$$m_i v_{cn} - m_i v_{in}(t) = \langle f_N \rangle_C \delta t_1 + \langle F_{in}^e \rangle_C \delta t_1 \qquad \text{compression}, \tag{e}$$

$$m_j v_{cn} - m_j v_{jn}(t) = \langle -f_N \rangle_C \delta t_1 + \langle F_{jn}^e \rangle_C \delta t_1 \qquad \text{compression}, \tag{f}$$

$$m_i v_{in}(t+\delta t) - m_i v_{cn} = \langle f_N \rangle_R (\delta t - \delta t_1) + \langle F_{in}^e \rangle_R (\delta t - \delta t_1) \qquad \text{recovery}, \tag{g}$$

$$m_j v_{jn}(t+\delta t) - m_j v_{cn} = \langle -f_N \rangle_R (\delta t - \delta t_1) + \langle F_{jn}^e \rangle_R (\delta t - \delta t_1) \qquad \text{recovery}, \tag{h}$$

where the compression duration is assumed to be δt_1, the recovery duration thereby being $\delta t - \delta t_1$, v_{cn} being the common normal velocity at the end of the compression phase (leading to a zero relative normal velocity between the particles), and $\langle\cdot\rangle_C$, $\langle\cdot\rangle_R$ denote the averaged impulses over the compression and recovery phases respectively. Using now the definition of restitution coefficient in tees of the ratio of recovery impulse to compression impulse in the normal direction, we have,

$$e = \frac{\text{recovery impulse}}{\text{compression impulse}} = \frac{\int_{t+\delta t_1}^{t+\delta t} f_n dt}{\int_t^{t+\delta t_1} f_N dt} = \frac{\langle f_N \rangle_R (\delta t - \delta t_1)}{\langle f_N \rangle_C \delta t_1} \tag{i}$$

Multiplying Eq. (g) and (h) with m_j and m_i respectively, and eliminating v_{cn}, we obtain the compression impulse as follows:

$$\langle f_N \rangle_C \delta t_1 = \frac{1}{m_i + m_j} \left[m_i \langle F_{jn}^e \rangle_C \delta t_1 - m_j \langle F_{in}^e \rangle_C \delta t_1 \right] - \frac{m_i m_j}{m_i + m_j} \left[v_{in}(t) - v_{jn}(t) \right] \tag{j}$$

Additionally, we have the total contact impulse $\langle f_N \rangle \delta t = \langle f_N \rangle_C \delta t_1 + \langle f_N \rangle_R (\delta t - \delta t_1)$, and from the definition of restitution coefficient as in Eq. (i), we have $\langle f_N \rangle \delta t = (1+e) \langle f_N \rangle_C \delta t_1$. Using the expression obtained in Eq. (j), we finally obtain:

$$\langle f_N \rangle \delta t = \frac{1+e}{m_i + m_j} \left[m_i \langle F_{jn}^e \rangle_C \delta t_1 - m_j \langle F_{in}^e \rangle_C \delta t_1 \right] - \frac{(1+e) m_i m_j}{m_i + m_j} \left[v_{in}(t) - v_{jn}(t) \right] \tag{k}$$

Plugging these contact impulses in the momentum balance equations as in Eqs. (5) and (6), the velocity update expressions presented in Eqs. (8) and (9) can be directly obtained. Extending the same algebraic formulation for the collisional momentum balance for a particle–surface contact, we can write the particle linear momentum balance, take the dot product along the normal vector to the surface, and decompose the collision step into a compression and recovery phase respectively as follows:

$$m \mathbf{v}_c(t+\delta t) - m \mathbf{v}_c(t) = \int_t^{t+\delta t} \left[\mathbf{F}^c + \mathbf{F}^e\right] dt = \langle \mathbf{F}^c \rangle \delta t + \langle \mathbf{F}^e \rangle \delta t \tag{l}$$

$$m v_{cn}(t+\delta t) - m v_{cn}(t) = \langle f_N \rangle \delta t + \langle F_n^e \rangle \delta t \tag{m}$$

$$m\bar{v} - mv_{cn}(t) = \langle f_N \rangle_C \delta t_1 + \langle F_n^e \rangle \delta t_1 \qquad \text{compression} \tag{n}$$

$$mv_{cn}(t+\delta t) - m\bar{v} = \langle f_N \rangle_R (\delta t - \delta t_1) + \langle F_n^e \rangle (\delta t - \delta t_1) \qquad \text{recovery} \tag{o}$$

where $\bar{v}$ is again the common normal velocity at the end of the compression phase. Using the relation $\langle f_N \rangle \delta t = (1+e)\langle f_N \rangle_C \delta t_1$ as described earlier, and setting the common velocity $\bar{v}$ (which is the normal surface velocity $v_{surf,n}$) from Eq. (n) and (o), we obtain the final form of the average normal contact impulse:

$$\langle f_N \rangle \delta t = (1+e)\left[mv_{surf,n} - mv_{cn}(t) - \langle F_n^e \rangle \delta t_1 \right] \tag{p}$$

Once the normal impulses are obtained, the tangential impulses are estimated using the regularized friction model directly, as described in Section 2.1 and Section 2.2.

Appendix B. Supplementary material

Supplementary material related to this article can be found online at http://dx.doi.org/10.1016/j.jcp.2015.02.034.

References

[1] P.M. Martin, Handbook of Deposition Technologies for Films and Coatings: Science, Applications and Technology, William Andrew, 2009.
[2] P. Martin, Introduction to Surface Engineering and Functionally Engineered Materials, vol. 74, Wiley-Scrivener, 2011.
[3] P. Meakin, Computer simulation of growth and aggregation processes, in: On Growth and Form, Springer, 1986, pp. 111–135.
[4] H.E. Stanley, N. Ostrowsky, On Growth and Form, Springer, 1986.
[5] H. Ogihara, J. Xie, J. Okagaki, T. Saji, Simple method for preparing superhydrophobic paper: spray-deposited hydrophobic silica nanoparticle coatings exhibit high water-repellency and transparency, Langmuir, ACS J. Surf. Colloids 28 (10) (2012) 4605–4608.
[6] W.M. Sigmund, N.S. Bell, L. Bergström, Novel powder-processing methods for advanced ceramics, J. Am. Ceram. Soc. 83 (7) (2000) 1557–1574.
[7] J. Kruth, M. Leu, T. Nakagawa, Progress in additive manufacturing and rapid prototyping, CIRP Ann., Manuf. Technol. 47 (I) (1998) 525–540.
[8] J. Pattison, S. Celotto, R. Morgan, M. Bray, W. O'Neill, Cold gas dynamic manufacturing: a non-thermal approach to freeform fabrication, Int. J. Mach. Tools Manuf. 47 (3–4) (2007) 627–634.
[9] D.D. Gu, W. Meiners, K. Wissenbach, R. Poprawe, Laser additive manufacturing of metallic components: materials, processes and mechanisms, Int. Mater. Rev. 57 (3) (2012) 133–164.
[10] B. Derby, N. Reis, Inkjet printing of highly loaded particulate suspensions, MRS Bull. November (2003) 815–818.
[11] E. Tekin, P.J. Smith, U.S. Schubert, Inkjet printing as a deposition and patterning tool for polymers and inorganic particles, Soft Matter 4 (4) (2008) 703.
[12] Z. Zhang, C. Kleinstreuer, Airflow structures and nano-particle deposition in a human upper airway model, J. Comput. Phys. 198 (1) (2004) 178–210.
[13] I. Balásházy, W. Hofmann, T. Heistracher, Local particle deposition patterns may play a key role in the development of lung cancer, J. Appl. Physiol. 94 (5) (2003) 1719–1725.
[14] U. Fritsching, Spray Simulation: Modelling and Numerical Simulation of Sprayforming Metals, Cambridge Univ. Press, 2004.
[15] M. Li, P. Christofides, Multi-scale modeling and analysis of an industrial HVOF thermal spray process, Chem. Eng. Sci. 60 (13) (2005) 3649–3669.
[16] J. Mostaghimi, Modeling thermal spray coating processes: a powerful tool in design and optimization, Surf. Coat. Technol. 163–164 (2003) 1–11.
[17] A. Kout, T. Wiederkehr, H. Müller, Efficient stochastic simulation of thermal spray processes, Surf. Coat. Technol. 203 (12) (2009) 1580–1595.
[18] J.B. McLaughlin, Aerosol particle deposition in numerically simulated channel flow, Phys. Fluids A, Fluid Dyn. 1 (7) (1989) 1211.
[19] A. Li, G. Ahmadi, Dispersion and deposition of spherical particles from point sources in a turbulent channel flow, Aerosol Sci. Technol. 16 (4) (1992) 209–226.
[20] G. Kallio, M. Reeks, A numerical simulation of particle deposition in turbulent boundary layers, Int. J. Multiph. Flow 15 (3) (1989) 433–446.
[21] E. Matida, K. Nishino, K. Torii, Statistical simulation of particle deposition on the wall from turbulent dispersed pipe flow, Int. J. Heat Fluid Flow 21 (2000) 389–402.
[22] T. Pöschel, T. Schwager, Computational Granular Dynamics: Models and Algorithms, Springer, 2005.
[23] Antonio A. Munjiza, The Combined Finite-Discrete Element Method, John Wiley & Sons, ISBN 978-0-470-02017-3, 2004.
[24] A. Konstandopoulos, Deposit growth dynamics: particle sticking and scattering phenomena, Powder Technol. 109 (September 1999) (2000) 262–277.
[25] T. Zohdi, Numerical simulation of the impact and deposition of charged particulate droplets, J. Comput. Phys. 233 (2013) 509–526.
[26] K.L. Johnson, Contact Mechanics, Cambridge Univ. Press, 1987.
[27] J. Shäfer, S. Dippel, D.E. Wolf, Force schemes in simulations of granular materials, J. Phys. I 6 (1) (1996) 5–20.
[28] H. Hertz, Miscellaneous Papers, Macmillan, 1896.
[29] R. Mindlin, Compliance of elastic bodies in contact, J. Appl. Mech. 16 (1949) 259–268.
[30] O. Walton, R. Braun, Viscosity, granular temperature, and stress calculations for shearing assemblies of inelastic frictional disks, J. Rheol. 30 (5) (1986) 949–980.
[31] L. Vu-Quoc, X. Zhang, An accurate and efficient tangential force-displacement model for elastic frictional contact in particle flow simulations, Mech. Mater. 31 (4) (1999) 235–269.
[32] P. Haff, B. Werner, Computer simulation of the mechanical sorting of grains, Powder Technol. 48 (3) (1986) 239–245.
[33] P.A. Cundall, O.D.L. Strack, A discrete numerical model for granular assemblies, Geotechnique 29 (1) (1979) 47–65.
[34] T.I. Zohdi, An Introduction to Modeling and Simulation of Particulate Flows, vol. 4, SIAM, 2007.
[35] D. Arbelaez, T.I. Zohdi, D.A. Dornfeld, Modeling and simulation of material removal with particulate flows, Comput. Mech. 42 (5) (2008) 749–759.
[36] D. Arbelaez, T. Zohdi, D. Dornfeld, On impinging near-field granular jets, Int. J. Numer. Methods Eng. 80 (6–7) (2009) 815–845.
[37] T. Zohdi, On the dynamics of charged electromagnetic particulate jets, Arch. Comput. Methods Eng. 17 (2) (2010) 109–135.
[38] D. Stewart, Rigid-body dynamics with friction and impact, SIAM Rev. 42 (1) (2000) 3–39.
[39] K.G. Murty, Linear Complementarity, Linear and Nonlinear Programming, Heldermann, Berlin, 1988.
[40] J. Duran, Sands, Powders, and Grains: An Introduction to the Physics of Granular Materials, Springer-Verlag, 2000.
[41] J.T. Oden, E.B. Pires, Nonlocal and nonlinear friction laws and variational principles for contact problems in elasticity, J. Appl. Mech. 50 (March 1983).
[42] P. Wriggers, G. Zavarise, Computational Contact Mechanics, Wiley Online Library, 2002.
[43] W. Goldsmith, Impact, the Technology and Physics Behavior of Colliding Solids, Dover, New York, 2001.
[44] S. Elghobashi, On predicting particle-laden turbulent flows, Appl. Sci. Res. 52 (4) (1994) 309–329.
[45] O. Druzhinin, S. Elghobashi, Direct numerical simulations of bubble-laden turbulent flows using the two-fluid formulation, Phys. Fluids 10 (3) (1998) 685–697.

[46] A. Ferrante, S. Elghobashi, On the physical mechanisms of two-way coupling in particle-laden isotropic turbulence, Phys. Fluids 15 (2003) 315.
[47] J. Ferry, S. Balachandar, A fast Eulerian method for disperse two-phase flow, Int. J. Multiph. Flow 27 (2001) 1199–1226.
[48] S. Balachandar, J.K. Eaton, Turbulent dispersed multiphase flow, Annu. Rev. Fluid Mech. 42 (2010) 111–133.
[49] A. Haider, O. Levenspiel, Drag coefficient and terminal velocity of spherical and nonspherical particles, Powder Technol. 58 (1) (1989) 63–70.
[50] L. Pawlowski, The Science and Engineering of Thermal Spray Coatings, John Wiley & Sons, 2008.
[51] S. Yuu, N. Yasukouchi, Y. Hirosawa, T. Jotaki, Particle turbulent diffusion in a dust laden round jet, AIChE J. 24 (3) (2004) 509–519.
[52] R. Bradley, The cohesive force between solid surfaces and the surface energy of solids, Lond. Edinb. Dublin Philos. Mag. J. Sci. 13 (86) (1932) 853–862.
[53] H. Hamaker, The London van der Waals attraction between spherical particles, Physica 4 (10) (1937) 1058–1072.
[54] J.N. Israelachvili, Intermolecular and Surface Forces, Academic Press, 2011.
[55] B.V. Derjaguin, Friction and adhesion. IV. The theory of adhesion of small particles, Kolloid-Z. 69 (1934) 155–164.
[56] S. Wall, W. John, H. Wang, S. Goren, Measurements of kinetic energy loss for particles impacting surfaces, Aerosol Sci. Technol. (June 2012) (1990) 37–41.
[57] C.T. Crowe, J.D. Schwarzkopf, M. Sommerfeld, Y. Tsuji, Multiphase Flows with Droplets and Particles, CRC Press, 2011.
[58] C. Ericson, Real-Time Collision Detection, CRC Press, 2004.
[59] G.S. Grest, B. Dünweg, K. Kremer, Vectorized link cell Fortran code for molecular dynamics simulations for a large number of particles, Comput. Phys. Commun. 55 (3) (1989) 269–285.
[60] A.A. Chialvo, P.G. Debenedetti, On the use of the Verlet neighbor list in molecular dynamics, Comput. Phys. Commun. 60 (2) (1990) 215–224.
[61] L. Verlet, Computer experiments on classical fluids. I. Thermodynamical properties of Lennard-Jones molecules, Phys. Rev. 159 (1) (1967) 98–103.
[62] H. Sigurgeirsson, A. Stuart, W.-L. Wan, Algorithms for particle-field simulations with collisions, J. Comput. Phys. 172 (2) (2001) 766–807.
[63] A. Donev, S. Torquato, F.H. Stillinger, Neighbor list collision-driven molecular dynamics simulation for nonspherical hard particles. I. Algorithmic details, J. Comput. Phys. 202 (2) (2005) 737–764.
[64] G. Sutmann, V. Stegailov, Optimization of neighbor list techniques in liquid matter simulations, J. Mol. Liq. 125 (2–3) (2006) 197–203.
[65] M.C. Sukop, D.T. Thorne Jr., Lattice Boltzmann Modeling: An Introduction for Geoscientists and Engineers, Springer Publishing Company, Incorporated, 2007.
[66] C.E. Chidume, Iterative approximation of fixed points of Lipshitzian strictly pseudo-contractive mappings, Proc. Am. Math. Soc. 99 (2) (1987) 283–288.
[67] X. Weng, Fixed point iteration for local strictly pseudo-contractive mapping, Proc. Am. Math. Soc. 113 (1991) 727–731.
[68] A. Berlemont, P. Desjonqueres, G. Gouesbet, Particle Lagrangian simulation in turbulent flows, Int. J. Multiph. Flow 16 (1) (1990) 19–34.
[69] S. Rentsch, R. Pericet-Camara, G. Papastavrou, M. Borkovec, Probing the validity of the Derjaguin approximation for heterogeneous colloidal particles, Phys. Chem. Chem. Phys. 8 (21) (2006) 2531–2538.
[70] B. Mishra, C. Murty, On the determination of contact parameters for realistic DEM simulations of ball mills, Powder Technol. 115 (3) (2001) 290–297.
[71] C. González-Montellano, A. Ramirez, E. Gallego, F. Ayuga, Validation and experimental calibration of 3d discrete element models for the simulation of the discharge flow in silos, Chem. Eng. Sci. 66 (21) (2011) 5116–5126.
[72] U. Zafar, C. Hare, A. Hassanpour, M. Ghadiri, Drop test: a new method to measure the particle adhesion force, Powder Technol. 264 (2014) 236–241.
[73] S.V. Klinkov, V.F. Kosarev, M. Rein, Cold spray deposition: significance of particle impact phenomena, Aerosp. Sci. Technol. 9 (7) (2005) 582–591.
[74] H. Assadi, F. Gärtner, T. Stoltenhoff, H. Kreye, Bonding mechanism in cold gas spraying, Acta Mater. 51 (15) (2003) 4379–4394.